journal of the mechanical behavior of biomedical materials 112 (2020) 104089

Contents lists available at ScienceDirect

Journal of the Mechanical Behavior of Biomedical Materials

journal homepage: http://www.elsevier.com/locate/jmbbm

Research Paper

Transient swelling behavior of the bovine caudal disc

Semih E. Bezci [a], Kyelo Torres [a], Carlo Carraro [b], Dominic Chiavacci [a], Ben Werbner [a], Shiyin Lim [a], Grace D. O'Connell [a,c,*]

[a] Department of Mechanical Engineering University of California, Berkeley, United States
[b] Department of Chemical and Biomolecular Engineering University of California, Berkeley, United States
[c] Department of Orthopaedic Surgery University of California, San Francisco, United States

ARTICLE INFO

Keywords:
Intervertebral disc
Bovine disc
Swelling
Residual strain
Image analysis
Digital image correlation

ABSTRACT

The intervertebral disc is an avascular composite structure, comprised of the nucleus pulposus (NP) and the annulus fibrosus (AF). Previous tissue-level experiments either examined relative differences in swelling capacity of the two disc regions at a single time point or tested explant structures that did not replicate *in situ* boundary conditions. Previous joint-level studies that investigated time-dependent fluid flow into the disc provided limited information about swelling-induced intradiscal strains with respect to time and boundary constraints. Therefore, the objective of this study was to investigate time-dependent swelling behavior of the intervertebral disc *ex situ*. The first study investigated time-dependent free-swelling response of the whole disc and the disc's sub-components separately (*i.e.,* NP and AF). Findings from this study showed that the swelling rate and swelling capacity of NP explants under free-swelling conditions were greater than AF explants. The second study evaluated the effect of boundary conditions on in-plane strain distributions of intact discs and AF rings. Swelling-induced strain was highly heterogeneous in AF rings, where negative circumferential strains were observed in the inner AF and tensile circumferential strains were observed in the outer AF. Radial strains in AF rings were an order of magnitude greater than circumferential strains. Restricting fluid flow only to the outer AF periphery reduced the swelling of the inner AF. Swelling of intact discs affected both NP and AF swelling behaviors, where NP hydration decreased by 60%. Furthermore, the presence of the NP reduced peak radial strains in the AF and resulted in uniform strain distribution throughout the AF. In conclusion, these studies highlight that tissue hydration and swelling-induced strains largely depend on regional biochemical composition and geometric boundary constraints.

1. Introduction

The intervertebral disc is an avascular heterogeneous composite structure, comprised of the nucleus pulposus (NP), a soft hyperelastic material that represents 40–50% of the disc volume, which is circumferentially encapsulated by the stiffer annulus fibrosus (AF) (Iatridis et al., 2007; O'Connell et al., 2007). Tissue composition varies spatially throughout the disc, with water accounting for 70–85% of the tissue's wet weight (Antoniou et al., 1996; Cortes et al., 2014; Iatridis et al., 2007). Moreover, both the NP and the AF have a tendency to absorb water and increase its volume by more than 50% (Bezci et al., 2019, 2015; Urban and Maroudas, 1981). The NP has higher water content and swelling capacity than the AF, and previous studies have associated differences in water content and swelling capacity to the higher concentration of negatively charged glycosaminoglycans (GAGs) in the NP (Bezci et al., 2015; Perie et al., 2006; Urban et al., 1979). Previous tissue-level experiments either examined relative differences in swelling capacity of the two disc regions at a single time point or tested explant structures that did not replicate *in situ* boundary conditions (*e.g.,* annular ring versus AF explant) (Bezci et al., 2019, 2015; Cortes et al., 2014; Oftadeh et al., 2018; Tavakoli, 2017; Urban and Maroudas, 1981). Hence, these findings provide limited understanding of the complex fluid-flow kinematics throughout the disc.

Mechanical loading causes complex deformations that induce interstitial fluid redistribution within the disc and fluid flow across the boundaries at the annulus periphery and endplates. Upon the removal of high loading, intradiscal pressure increases as disc absorbs water and regains disc height (Bezci and O'Connell, 2018; Reitmaier et al., 2012;

* Corresponding author. University of California, Berkeley Department of Mechanical Engineering, 5122 Etcheverry Hall, #1740, Berkeley, CA, 94720, United States.
E-mail address: g.oconnell@berkeley.edu (G.D. O'Connell).

https://doi.org/10.1016/j.jmbbm.2020.104089
Received 2 February 2020; Received in revised form 8 September 2020; Accepted 10 September 2020
Available online 22 September 2020

Vergroesen et al., 2014). Direct measurement of fluid distribution within the disc is challenging. Hence, recent research used quantitative magnetic resonance imaging to measure regional changes in intradiscal water content with diurnal loading (Martin et al., 2018 – in review). Joint-level *in vitro* studies monitored disc height or intradiscal pressure to indirectly determine the direction, magnitude, and rate of fluid flow during physiological loading conditions. These studies observed differences in fluid-flow kinematics with osmotic loading, loading conditions (*i.e.*, mode, magnitude, rate and frequency), age, and degeneration (Bezci and O'Connell, 2018; MacLean et al., 2007; O'Connell et al., 2011; van der Veen et al., 2007). However, these observations were limited to the changes for the entire bone-disc-bone motion segment, providing a lack of understanding of mechanisms for complex intradiscal fluid flow behavior during recovery. Recent advancements in image-processing algorithms have made optical, non-contact measurement techniques appealing for investigating local tissue strains.

Swelling capacity and swelling-induced tissue deformations highly depend on the boundary conditions (Yang and O'Connell, 2019). Healthy discs hydrated after removal of the endplates and vertebral bodies experience a 50–60% increase in tissue mass, and the relative effect of the endplate boundary condition decreases with degeneration due to decreased swelling capacities of both the NP and inner AF (Jim et al., 2011; Yang and O'Connell, 2019). The effect of boundary condition is greater for tissue explants, where testing NP-only specimens results in significant increases in tissue weight under stress-free boundary conditions (Bezci et al., 2015). Specifically, the swelling ratio, defined as the increase in tissue weight due to swelling divided by the initial weight, decreases linearly from 1.85 at the disc center (*i.e.,* 185% increase in NP tissue weight) to 0.5 in the outer AF (Bezci et al., 2019).

Thus, fluctuations in water content due to diurnal loading or compositional changes with degeneration play an important role in intradiscal strain distributions during loading (Botsford et al., 1994; Martin et al., 2018). Low tissue permeability hinders fluid flow, making disc height recovery a slow time-dependent process that is dependent on loading history and the osmotic differential between the tissue and surrounding environment (Bezci and O'Connell, 2018; O'Connell et al., 2011; Schmidt et al., 2016). As a result, discs *in vivo* and *in vitro* can achieve different levels of hydration, which affect relative joint stiffness (Bezci et al., 2015; Schmidt et al., 2016). Despite numerous joint-level studies that investigated the time-dependent fluid-flow behavior, there is limited understanding of swelling-induced intradiscal strain distributions with respect to swelling time and boundary conditions. Therefore, the objective of this study was to investigate time-dependent swelling behavior of the intervertebral disc *ex situ.*

2. Material and methods

Two separate experiments were performed to evaluate time-dependent swelling behavior of the intervertebral disc *ex situ*. The first objective was to investigate free-swelling behavior of the whole disc and disc subcomponents separately (*i.e.*, AF- or NP-only explants; Fig. 1A). The second objective was to evaluate the effect of swelling boundary conditions on in-plane strain distributions of intact discs and discs with the NP removed (annular rings; Fig. 1B). The first group consisted of AF rings in contact with saline at the outer periphery and at the center of the annular ring (Fig. 1B – left, blue arrows). The second group included AF rings in contact with saline solution only at the outer periphery. Finally, the third group included intact discs in contact with saline at the outer periphery.

Fresh-frozen bovine tails were obtained from a local abattoir (13 spines, age: 16–18 months) and defrosted in 0.15 M phosphate-buffered saline solution (PBS) at room temperature. Following the removal of surrounding musculature and ligaments, bovine discs were isolated from the adjacent vertebrae with a scalpel and only the top three levels were used for testing (C2 – C4). Discs were visually examined for signs of damage (damage observed in 4/42 discs). Intact, healthy discs were

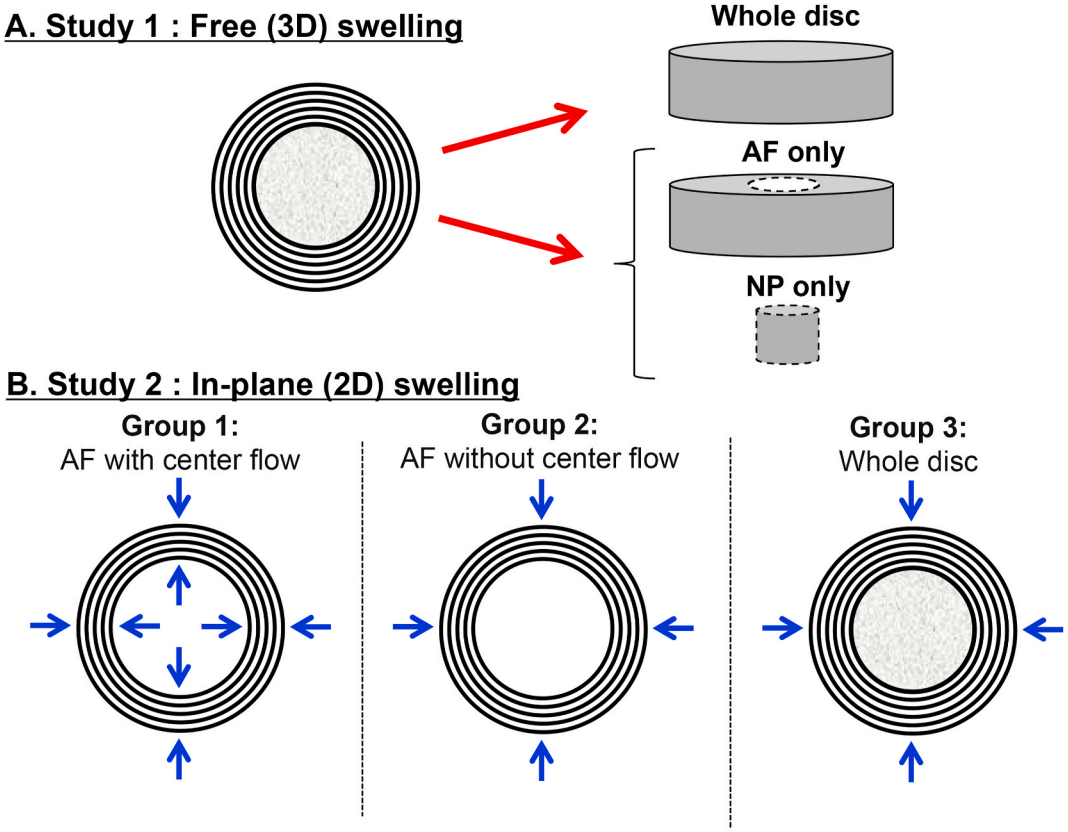

Fig. 1. Study design for (A) free (3D) and (B) in-plane (2D) swelling experiments. Blue arrows represent expected fluid flow due to contact with saline solution.

selected, wrapped with a saline-soaked gauze and stored frozen at −20°C.

2.1. Free-swelling experiment

Prior to testing, discs were thawed at room temperature. NP sections were harvested from the disc center with a biopsy punch (diameter = 10 mm; Fig. 1). Residual NP tissue was removed from the AF ring with a scalpel. Free-swelling behaviors of the intact discs, AF rings, and cylindrical NP explants were investigated by immersing samples in 0.15 M PBS for 16 h (n = 7 per group). To quantify swelling, tissue wet-weight was measured before swelling. Specimens were weighed every 15 min during the first 2 h of swelling and weighed hourly after the initial 2-h period. Before measuring sample weight, excess surface water was removed by gently blotting the tissue with a kimwipe.

The swelling ratio (Q) was calculated as the change in tissue weight during swelling with respect to initial wet weight (or pre-swelling wet weight) divided by the initial wet weight (*i.e.*, $Q = 100 \times (m_i - m_o)/m_o$). A stretched exponential function was used to describe swelling ratio as a function of time (Equation (1)), where model parameter Q_{eq} represents equilibrium swelling ratio (unitless), τ is the time constant (hours), and β is the stretch parameter to describe nonlinearity (unitless; bounded between 0 and 1) (Van der Veen et al., 2013). Preliminary work showed that this simplified model was sufficient for predicting equilibrium behavior of tissue explants and did not overestimate of equilibrium behavior, as observed for time-dependent behavior of bone-disc-bone motion segments (Van der Veen et al., 2013).

$$Q(t) = Q_{eq}\left(1 - e^{-(t/\tau)^{\beta}}\right) \quad (1)$$

2.2. In-plane (2D) swelling experiment

For 2D in-plane swelling experiments, discs were shaved with a temperature-controlled freezing stage microtome to create parallel surfaces (n = 8–9 per group; Leica SM2400, Leica Biosystems Inc., IL, USA). After obtaining parallel surfaces, sample height was measured using a digital caliper and specimens were thawed at room temperature for speckle patterning. For AF ring specimens, the NP was removed with a scalpel. To facilitate the digital image correlation (DIC) analysis, India ink was airbrushed onto the top surface to create a speckle pattern (Fig. 2A). A nozzle diameter of 0.3 mm was chosen to obtain an average speckle size exceeding the image pixel size by a factor of 3–5 (Lionello and Cristofolini, 2014; Zhou et al., 2016).

2D planar swelling experiments were performed in a custom-built swelling chamber filled with 0.15 M PBS (Fig. 2). An adjust lamp was used for illumination during testing. To perform 2D strain analyses, swelling in the z-direction (out-of-plane motion) was restricted with a transparent glass lid (thickness = 2.45 mm, mass = ~20 g; Fig. 2 – side view). Screws to affix the glass lid were evenly spaced and the height of the lid was secured using nuts (120° apart; Fig. 3 – top view).

A digital monochrome camera equipped with a 75 mm lens was used to acquire images for 16 h (Fujifilm, USA, 1 frame/minute; 1920 × 1200 pixels, Grasshopper 3 USB3, Model: GS3-U3-23S6M-C; FLIR Systems, Inc., USA). DIC analysis was performed using commercial software to calculate in-plane displacements and Lagrangian strains (ε_{xx}, ε_{yy}, and ε_{xy}) (subset size = 111 pixels, step size = 5 pixels, incremental correlation; Vic-2D, Correlated Solutions Inc., Columbia SC). DIC data were post-processed using a custom-written MATLAB algorithm (Mathworks Inc, Natick MA). First, the disc edge and the boundary between the NP and AF were manually selected (O'Connell et al., 2007). Based on the boundary selection, disc center and cross-sectional area were calculated and DIC data for pixels located outside of the disc edge were discarded from further analysis. To remove any outliers, principal strains that were ±3 standard deviations away from the mean were eliminated (~5%). Next, radial displacement was calculated for each pixel by calculating the difference between the final and initial radial locations with respect to the origin, which was defined as the disc center. Strain components were transformed from Cartesian to polar coordinates using the rotation of axes.

Test specimens were digitally segmented to identify the region-specific differences in swelling behavior. In all three experimental groups, the AF was divided into three concentric rings with equal thickness to describe region-dependent strains in the inner AF (IAF), middle AF (MAF) and outer AF (OAF). For intact discs, the NP was analyzed as a single region of interest. Mean radial and circumferential strain values were calculated for each region.

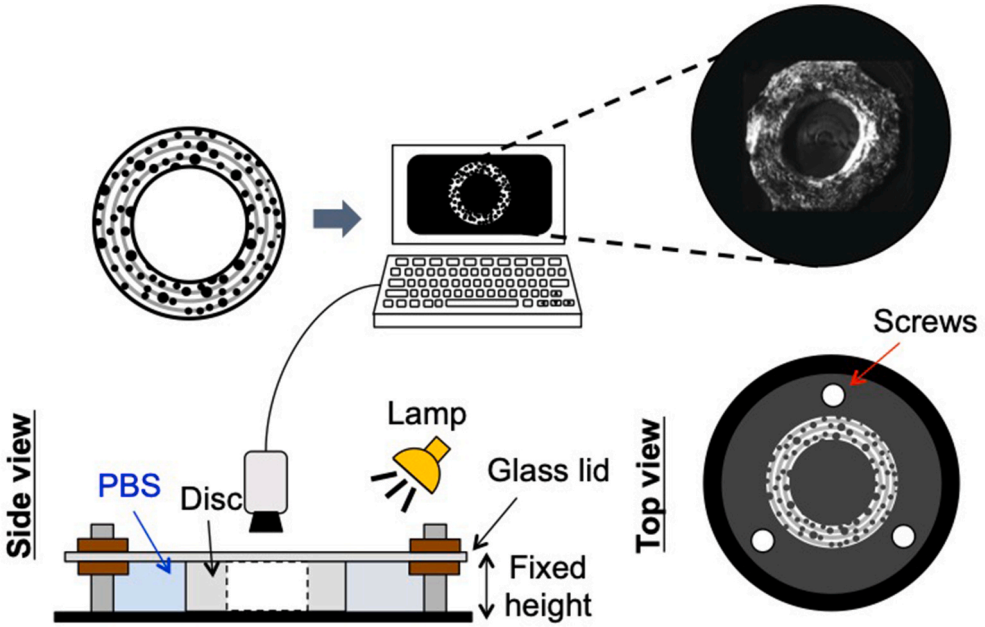

Fig. 2. Schematic of experimental set-up for in-plane (2D) swelling experiments. A speckle pattern was applied to the top surface of the whole discs and AF rings before submerging them in saline for 16 h. Disc height was fixed to avoid out-of-plane motion.

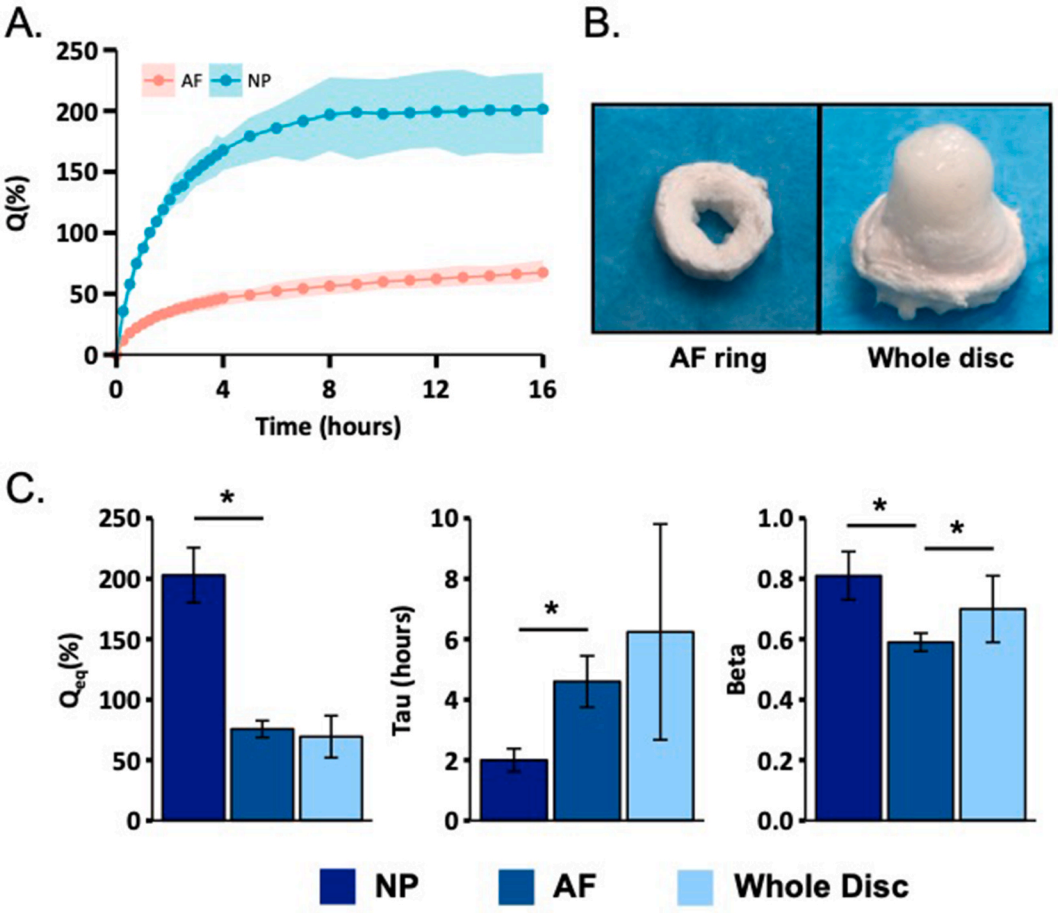

Fig. 3. A) AF (red) and NP (blue) swelling ratio throughout the 16-h free swelling period. Shaded area represents the range (minimum to maximum) of experimental data. B) Representative images of a swollen AF ring and intact disc. C) Parameters for the stretched exponential function. Comparisons are made between the NP and the AF, and between the AF and whole disc. * represents $p < 0.05$. Error bars represent one standard deviation.

2.3. Water content analysis

2.3.1. Gravimetric water content measurement

After swelling experiments were completed, test specimens were freeze-dried in a lyophilizer for 72 h to measure specimen dry weight. For intact discs in free-swelling experiments, the NP was separated from the AF using a scalpel. The NP explants and AF rings obtained from the intact discs were weighed to measure swollen tissue weight and freeze-dried separately to make comparisons with the water content measurements for tissue explants. Water content of the test specimens in this study was calculated as the difference between the swollen wet weight and dry weight normalized by dry weight. For specimens in the 2D swelling experiment, a 4 mm biopsy punch was used to obtain cylindrical tissue samples from the inner NP (INP) and the outer NP (ONP). Additionally, AF tissue strips with dimensions of 4 mm × 2 mm along the sample thickness were acquired from the inner AF and outer AF. The AF was separated into two regions for biochemical analysis, instead of three as in the swelling analyses, to compare post-swelling water content measurements with pre-swelling water content data previously reported by our laboratory (Bezci et al., 2019). Water content of the test specimens was calculated as the difference between the swollen wet weight (WW) and dry weight (DW) normalized by swollen wet weight or dry weight to compare results across data reported in the literature. Duplicate measurements for each NP or AF region were averaged for statistical analysis.

2.3.2. Raman-based water content measurement

Three cylindrical NP and AF ring tissue samples were randomly chosen from the first study for qualitative assessment of swelling capacity using Raman spectroscopy (excitation at 632.8 nm; Horiba Jobin Yvon Labram spectrometer with Olympus BX41 confocal microscope). Raman spectra of each sample were collected in triplets over a frequency range of 2800–3800 cm^{-1}, and average spectra were calculated for the swollen NP and AF tissues. Representative spectra for swollen tissue samples were compared to spectra for bovine NP and AF samples before swelling (Bezci et al., 2019). Spectra were normalized to have the same intensity signal at 2945 cm^{-1}, which corresponds to CH_3 stretching vibrations in proteins and lipids, and thus is unaffected by hydration (Parkes et al., 2017).

2.4. Statistics

All statistical analyses were performed in R (R Project for Statistical Computing, Vienna, Austria), with significance assumed for $p < 0.05$. For Study 1, time-dependent changes in the swelling ratio were reported for the 16-h period. Swelling ratios of the intact disc, AF, and NP specimens were compared using a one-way analysis of variance (ANOVA). Pairwise comparisons were made between the NP and the AF, and between the AF and the whole disc. For Study 2, the average disc height and area were calculated for each experimental group and compared using a one-way ANOVA to ensure comparable disc geometry across groups. Mean strain values were calculated at 2, 8, and 16 h of swelling. For each experimental group, a two-way ANOVA was performed to determine the effect of swelling time and region on swelling-induced strains. Additionally, a separate two-way ANOVA was conducted to assess the influence of the fluid boundary conditions on tissue strain for

each annular region (factors = fluid boundary condition and annular region = IAF, MAF, and OAF). Whenever significance was detected, a Tukey post-hoc analysis was performed to compare groups.

Post-swelling water contents of the inner and outer NP were compared with previous pre-swelling water content data using an unpaired Student's t-test (Bezci et al., 2019). Separate one-way ANOVA analyses were conducted for each AF region to assess differences in post-swelling water content across four different testing conditions. The Bonferroni correction method was used to account for multiple comparisons.

3. Results

3.1. Free-swelling experiment

Swelling ratio (Q) changed nonlinearly with time for all tissue types, and the majority of swelling was observed during the first 4 h (Fig. 3A). After 16 h of free swelling, the final swollen weight of NP explants was 200% greater than the initial wet weight, while the final swollen weight of AF rings was 60% greater than the initial wet weight (Fig. 3A – blue versus red curves). Importantly, AF rings retained their ring shape during swelling. However, the additional boundary constraint of the AF onto the NP caused significant deformations along the axial direction during swelling, resulting in a disc that resembled a sewing thimble (Fig. 3B).

The water content of the cylindrical NP tissue explants after swelling was 2.5 times the water content of NP in intact discs (i.e., 21.6 ± 2.9 g/g DW versus 8.5 ± 1.3 g/g DW). Similarly, the water content of the AF rings after swelling was 1.4 times the water content of the AF in intact discs (i.e., 4.35 ± 0.26 g/g DW versus 3.05 ± 0.30 g/g DW).

There was a significant difference in model parameters that described NP explant swelling behavior compared to parameters that described AF swelling behavior ($p < 0.001$; Fig. 3C). Specifically, the equilibrium swelling ratio (Q_{eq}) of NP explants was 2.7 times the AF Q_{eq} ($p < 0.001$; Fig. 3C). Q_{eq} of intact discs was not statistically different from Q_{eq} of the AF explants ($p = 0.4$). The time constant (τ) was lower for the NP than the AF, suggesting a higher swelling rate for the NP ($p < 0.001$). Due to the variation in τ for the whole disc, no significant differences were observed between the intact disc and tissue explants. The stretch parameter (β) for NP explants and intact discs was 20–40% greater than β for AF rings ($p < 0.03$).

Raman spectra showed that the signal intensity for wavelengths above ~3000 cm^{-1} increased with swelling in both the NP and the AF (Fig. 4; solid versus dotted lines). Similar to observations from gravimetric measurements, the change in signal intensity was greater for the NP than the AF (Fig. 4; red versus black lines). After swelling, water spectrum (>3000 cm^{-1}) for the AF was similar to the spectrum for the NP before swelling.

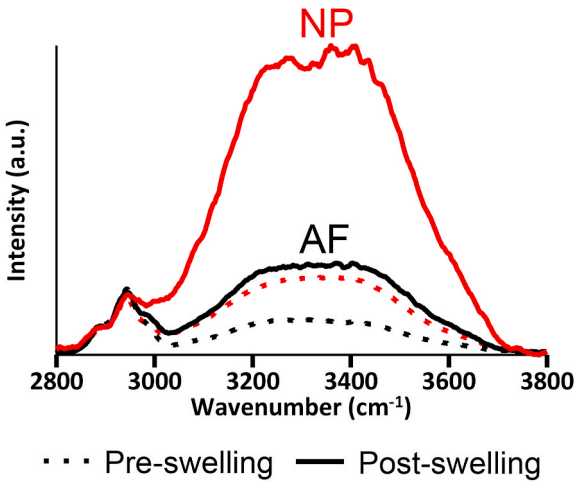

Fig. 4. Comparison of Raman specta pre- (dashed lines) and post-swelling (solid lines) for the nucleus pulposus (NP; red lines) and annulus fibrosus (AF; black lines).

3.2. In-plane (2D) swelling experiment

Discs used for the three experimental groups were comparable in height and area ($p > 0.5$, height = 5.40 ± 0.68 mm, area = 473 ± 58 mm^2). For AF rings, removed NP tissue corresponded to 51 ± 3% of the total area.

For AF rings with fluid flow from both the center and outer annular periphery, there was a nonlinear relationship between radial and circumferential strains with swelling time (Fig. 5A and B – Group 1). In general, radial strains were an order of magnitude greater than circumferential strains. All AF regions experienced positive radial strains during swelling, with the magnitude of radial strains being highest in the inner AF for all time points ($p < 0.001$ for region; Fig. 5A–C). There was a significant increase in average radial strains with swelling time for all AF regions ($p \leq 0.014$). After 16 h, mean radial strain was approximately 0.65 mm/mm (or 65%) in the inner AF and 0.10 mm/mm (or 10%) for the outer AF (Fig. 5C). Negative circumferential strains were observed in the inner AF, while positive circumferential strains were observed in the outer AF. Circumferential strains in the middle and inner AF did not change after 2 h of swelling ($p \geq 0.2$) and after 8 h in the outer AF. After 16 h of swelling, the average circumferential strain was slightly compressive (−0.04 mm/mm or −4%) in the inner AF and slightly tensile (<0.02 mm/mm or 2%) in the middle and outer AF (Fig. 5D).

Restricting fluid flow to only the AF periphery greatly altered swelling behavior (Fig. 5C and D *versus* Fig. 6A and B). Similar to the AF rings in Group 1, radial and circumferential strains for AF rings in Group 2 increased with time. As expected, the greatest changes in swelling behavior were observed in the inner AF, where radial strains decreased from 0.65 mm/mm in Group 1 to ~0.07 mm/mm when fluid was absent (90% decrease; Fig. 5C versus 6 A). Therefore, peak radial and circumferential strains in Group 2 occurred in the outer AF (Fig. 6A and B). The behavior of circumferential strains with respect to annular region was not affected by the change in fluid flow. That is, circumferential strains in the inner AF were slightly negative, while circumferential strains in the outer AF were positive (Fig. 6B). Radial and circumferential strains for the outer AF in Group 2 were similar to radial and circumferential strains for the outer AF in Group 1. Radial and circumferential strains in the outer AF were stable after 2 h of swelling ($p \geq 0.09$). In contrast, inner AF radial and circumferential strains at 16 h were greater than strains measured after 2 h of swelling ($p < 0.05$).

For intact discs (Group 3), strain analysis was initially performed on three separate AF regions to identify spatial differences within the AF; however, no significant differences were observed for circumferential or radial strains (two-way ANOVA, $p > 0.1$). Therefore, AF data were pooled and reported for each time point (Fig. 7). Within 2 h of swelling, the NP experienced negligible radial and circumferential strains (<0.01 mm/mm or 1%), but the magnitude of radial and circumferential strains continued to increase throughout 16-h swelling period (Fig. 7 - red dots). After 16 h, average NP radial strain was 0.08 mm/mm and the average circumferential strain was 0.04 mm/mm. In the AF, radial strains were consistent after 8 h of swelling (~0.06 mm/mm; Fig. 7A – blue dots). In contrast, circumferential strains in the AF increased throughout the 16-h swelling period, with a two-fold increase between 8 and 16 h (Fig. 7B – blue dots). Circumferential strains in the AF of intact discs were 2–5 times greater than strains measured in AF rings (Fig. 7B *versus* Figs. 5D & 6B).

Similar trends were observed for water content normalized by wet and dry weights for most disc regions (Fig. 8A *versus* 8 B). Swelling capacity of the inner AF was highly sensitive to the fluid boundary condition (Fig. 8 – IAF). As expected, inner AF swelling capacity was

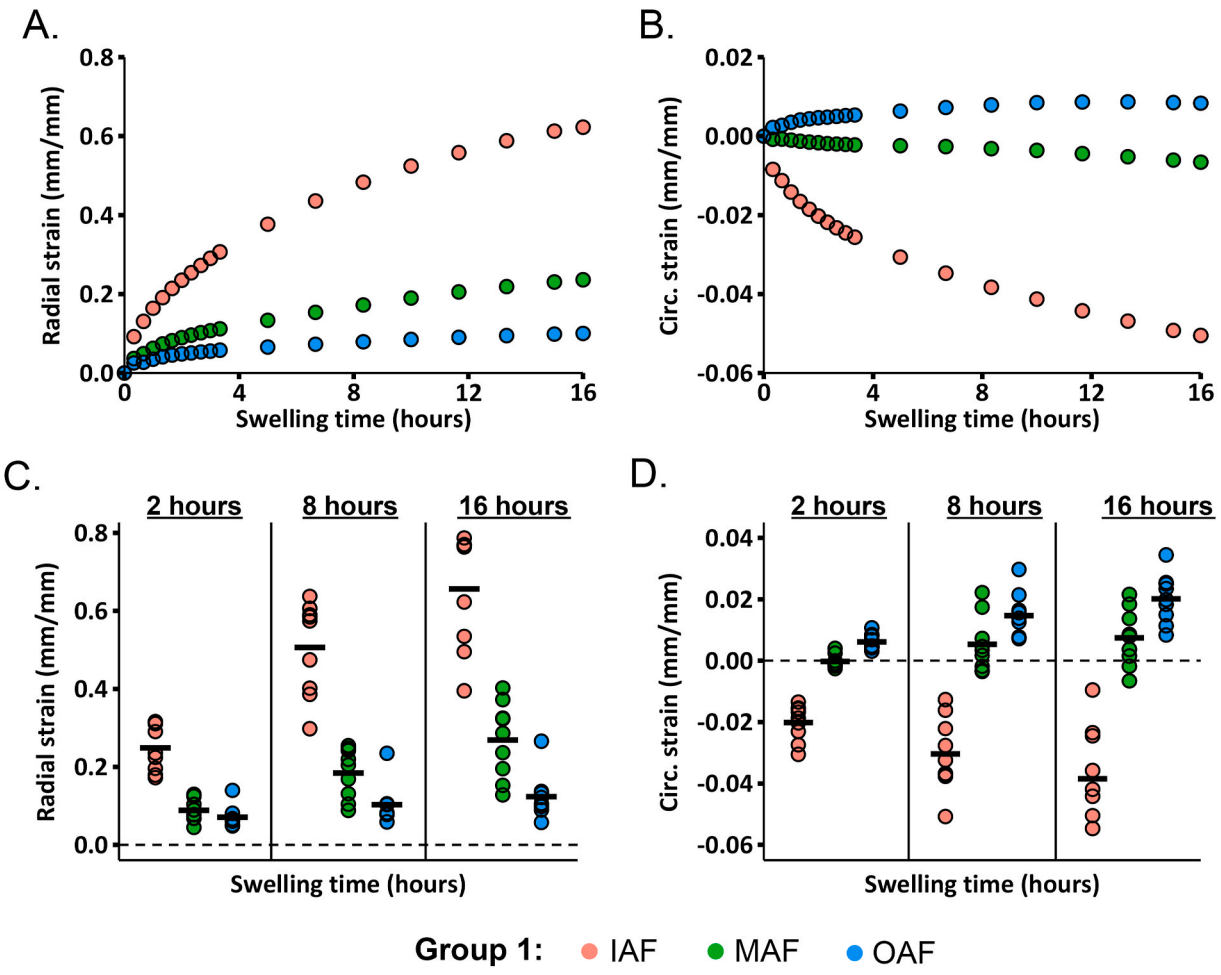

Fig. 5. Results for AF rings with fluid flow from the outer periphery and center. A) Radial and B) circumferential strains during the 16-h swelling period, shown for a representative sample. C) Radial and D) circumferential strains after 2, 8, and 16 h of swelling (n = 8 per group). Red, green, and blue dots represent data for the inner (IAF), middle (MAF), and outer (OAF) annulus fibrosus, respectively. Black lines indicate mean values and dashed lines represent zero strain.

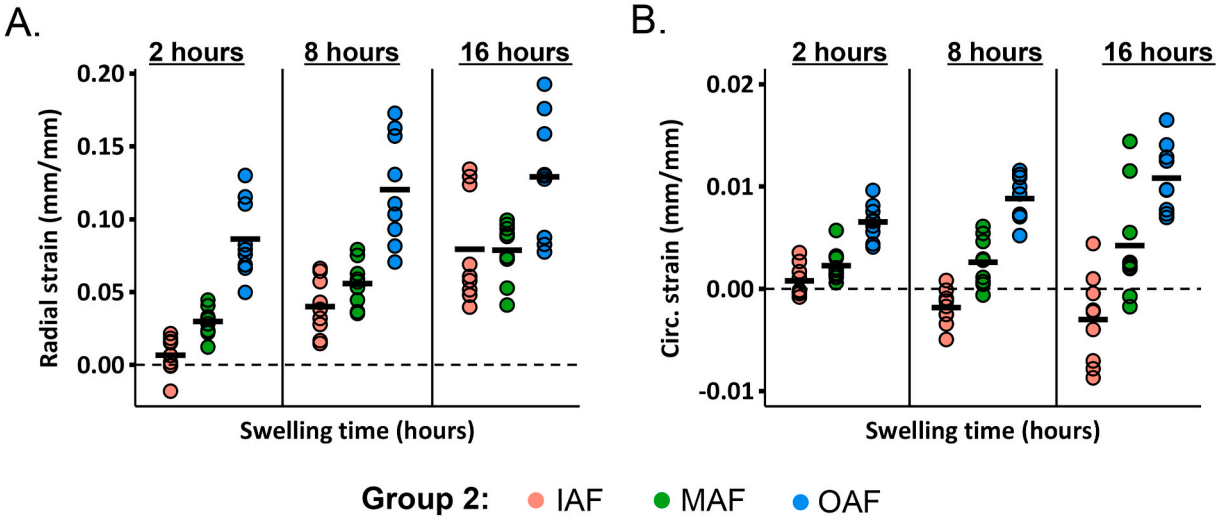

Fig. 6. A) Radial and B) circumferential strain measurements for AF rings without fluid flow from the center. Data were collected throughout the 16 h swelling period and analyzed at 2, 8 and 16 h (n = 9 per group). Red, green and blue colors represent data from the inner (IAF), middle (MAF) and outer (OAF) annulus fibrosus, respectively. Black lines indicate the mean values and the dashed lines represent zero strain.

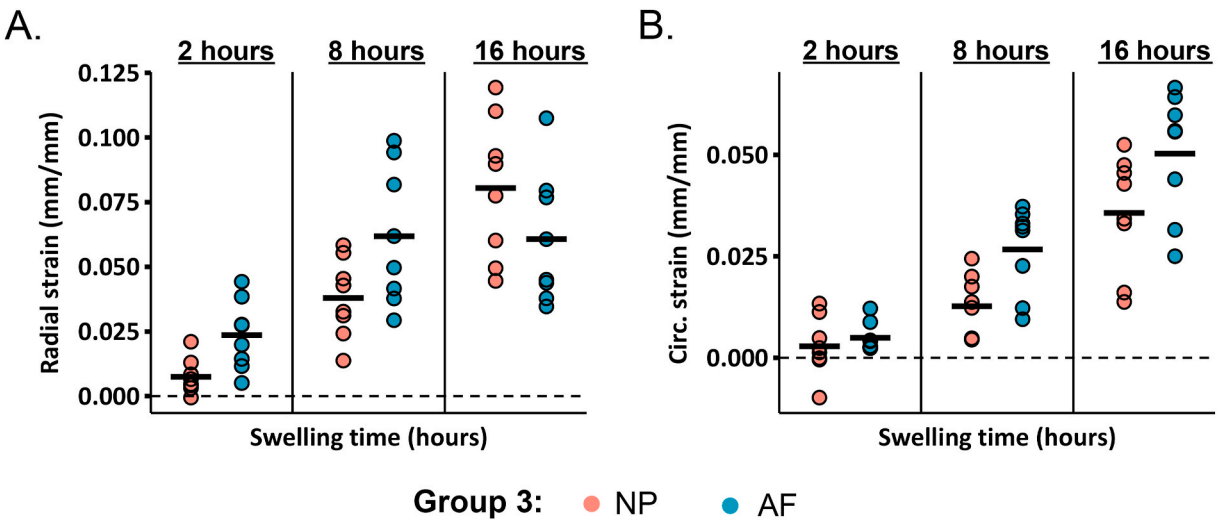

Fig. 7. A) Radial and B) circumferential strain measurements for intact discs. Data were collected throughout the 16 h swelling period, and analyzed at 2, 8 and 16 h (n = 8 per group). Red dots represent data from the nucleus pulposus (NP) and blue dots represents data from the annulus fibrosus (AF). Black lines indicate the mean values and the dashed lines represent zero strain.

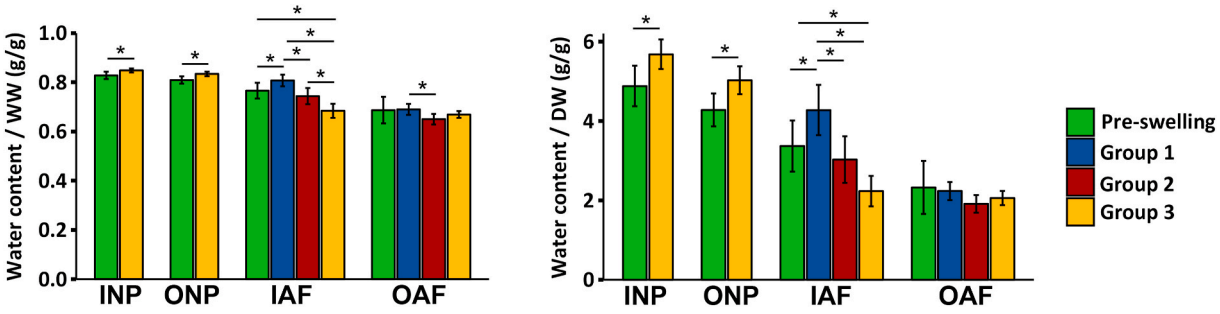

Fig. 8. Mean and standard deviation of pre- and post-swelling water content normalized by wet (left) and dry (right) weights. Pre-swelling measurements (green bars) represent data from our previous work (Bezci et al., 2019). Blue bars indicate the water content measurements for the AF rings with fluid flow from the center, and red bars represent water content measurements for the AF rings without fluid flow from the center. Yellow bars represent water content measurements for intact discs. * represents $p < 0.05$. Error bars represent one standard deviation.

greatest with direct access to fluid and was influenced by interactions with the NP and outer AF (Fig. 8 – blue bar *versus* yellow or red bars). Interestingly, post-swelling water contents of the inner and outer AF from Group 2 were not significantly different than pre-swelling water content (Fig. 8 – green *versus* red bars). For intact discs, both inner and outer NP absorbed water and increased tissue mass during swelling (Fig. 8A&B – green *versus* yellow bars).

4. Discussion

This study aimed to characterize the time-dependent swelling behavior of the intervertebral disc, rather than solely providing equilibrium properties after an extended swelling period. To achieve this, the first study monitored time-dependent changes in tissue mass to compare differences in the swelling behaviors of NP and AF explants under free swelling conditions. As expected, this study observed large differences in free swelling behaviors of the NP and AF tissue explants. However, observations from the first study and previous work that measured AF residual strains after swelling were limited to bulk tissue properties, disregarding complex *in situ* fluid flow behavior between the NP and AF (Michalek et al., 2012). To improve our understanding of localized changes during swelling, the second study quantified swelling-induced strains throughout the AF and intact discs. Positive radial strains were observed for all three experimental groups, suggesting radial thickening of intact discs or AF layers as a result of tissue swelling. Circumferential strains were more complex, with small or negative strains observed in the inner AF. Negative circumferential strains observed in the inner AF indicated circumferential shortening due to inward movement of the tissue. In contrast, circumferential strains in the middle and outer AF were positive, suggesting circumferential lengthening at the outer AF periphery.

NP explants experienced a higher swelling rate and equilibrium swelling capacity than AF explants. Specifically, there was a 200% increase in the NP tissue mass, agreeing with previous values reported for the NP, and a 70% increase in the AF tissue mass under free swelling conditions (Bezci et al., 2019, 2015). The difference between NP and AF swelling behaviors was also observed through relative changes in the Raman signal intensity (wavenumbers > 3000 cm^{-1}) of each tissue before and after swelling. This relative difference was expected based on previous observations that noted a decrease in tissue swelling capacity with decreases in GAG content from disc center to the outer periphery and with disc degeneration (Bezci et al., 2019, 2015; Urban and Maroudas, 1981; Werbner et al., 2019). However, the AF swelling capacity measured here was ~25% lower than previously measured values, most likely due to differences in boundary conditions, and 20% lower than expected values based on relative differences in NP and AF GAG contents (NP GAG = 319 ± 62 mg/g DW, AF GAG = 129 ± 36 mg/g DW) (Bezci et al., 2019, 2015). The discrepancy between expected and measured values for AF swelling capacity is partially due to the highly organized, dense collagen fiber architecture in the AF (Marchand and Ahmed,

1990), where collagen fibers counteract the swelling pressure generated by the proteoglycans and limit AF tissue swelling (Yang and O'Connell, 2019). Moreover, degradation of AF GAGs has shown to have limited impact on water content (90% GAG loss resulted in 10% decrease in water content), suggesting that AF porosity may be the primary mechanism for AF fluid flow rather than negatively charged GAGs (Werbner et al., 2019). Lastly, the highly organized fiber architecture in the AF provided shape stability during swelling, whereas NP explants swelled into amorphous blobs when removed from its *in situ* boundary conditions, possibly due to the random orientation of collagen fibers in the NP (Inoue, 1981).

Tissue swelling capacity was sensitive to changes in physical boundary conditions. Based on the water content measurements of the NP and the AF in free-swelling experiments, the swelling capacity of the NP decreased by 60% due to the boundary constraint imposed by the surrounding AF (i.e., from 21.6 ± 2.9 g/g DW to 8.5 ± 1.4 g/g DW). Additional boundary constraint due to fixed axial deformations further decreased NP tissue swelling capacity by 15% (i.e., to 5.35 g/g DW). Similarly, the swelling capacity of the AF decreased by 30% with the presence of the NP (i.e., from 4.35 ± 0.26 g/g DW to 3.1 ± 0.3 g/g DW) under free swelling conditions. The water content of the AF in intact discs (pooled averages of the inner and outer AF) was reduced by an additional 20% when axial deformation due to tissue swelling was restricted. These findings explain lower strain magnitudes reported here compared to computational results (Yang and O'Connell, 2019). During low loading recovery (*e.g.*, bed rest recovery), the disc height increases due to fluid flow into the disc and poroelastic recovery of the solid matrix (Bezci and O'Connell, 2018). Therefore, recovery of the solid matrix increases disc volume, allowing NP and AF tissues to swell further (Schroeder et al., 2006). These two mechanisms, poroelastic recovery and fluid flow recovery, act as a feedback loop until disc reaches the equilibrium hydration level.

Recent computational modeling using triphasic mixture theory to describe non-fibrous solid matrix of the intervertebral disc tissues demonstrated that radial changes in tissue swelling ratio are largely driven by spatial variations in GAG composition (Yang and O'Connell, 2019). Specifically, simulations of intact discs under swelling conditions predicted relatively uniform radial, axial, and circumferential strains (comparable to conditions in Group 3). Findings from the current study agree with previous observations, as initial analysis found no differences in AF strains; hence, pooled results were presented in Fig. 7. Radial distribution of AF GAGs acts to create radius-dependent residual strains, which is important for maintaining a homeostatic strain distribution with intradiscal pressure from the NP (Yang and O'Connell, 2019). Similarly, this previous computational study showed a linear decrease in tensile radial strains from the inner AF to the outer AF in annular rings with fluid exchange permitted at both the inner and outer AF boundaries (comparable to conditions in Group 1). Circumferential strains were reported to be compressive in the inner AF and tensile in the outer AF, which was confirmed by Group 1 findings in this study (Fig. 5). Findings from this study provide strong supportive data for computational model validation, which is often a significant challenge in the field of computational biomechanics (Zhou et al., 2019). These findings can aid future *in silico* studies to fine-tune the material properties and validate the accuracy of their hybrid disc models (NP + AF) before introducing additional factors, such as disc degeneration and aging.

Besides physical boundary constraints, restricting fluid flow only to the outer periphery further reduced the swelling rate and magnitude of the annular rings, especially in the inner AF (Group 1 *versus* Group 2). The rate of swelling was much slower in Group 2 than Group 1, where the path length for water to reach the inner AF is shorter. In contrast, time-dependent fluid flow to the outer AF was nearly identical in both experimental conditions. Largest radial strain was observed in the outer AF when fluid flow permitted only on the outer periphery (Group 2); however, there was no statistically significant increase in AF water content throughout the AF thickness. In contrast, the inner AF water content increased by 21% when fluid flow was allowed to occur simultaneously on the inner and outer tissue surfaces (Group 1), resulting in peak radial and circumferential strains in the inner AF, not in the outer AF. Higher GAG content in the inner AF allowed it to swell by a larger amount and with faster rate than the outer AF (Bezci et al., 2019). Regardless, both experimental groups had negative circumferential strain in the inner AF, but positive circumferential strain in the outer AF, agreeing with previous findings (Duclos and Michalek, 2017; Michalek et al., 2012). For AF rings, negative circumferential strains coupled with positive radial strains in the inner AF suggest that the inner AF moved inwards during swelling. However, large differences in the strain distributions between the two AF-ring groups might imply that boundary effects have a much stronger influence on AF tissue swelling than inhomogeneous GAG distribution.

NP pressurization during swelling restricted AF swelling capacity, resulting in uniform strain distribution throughout the AF. After 2 h of swelling, the NP experienced negligible radial and circumferential strains (<0.01 mm/mm or 1%), suggesting that fluid flow takes longer than 2 h to reach the disc center. After 16 h of swelling, the radial strains in the outer AF was ~0.1 mm/mm (or 10%), which was 50% lower than the radial strains in the outer AF of annular (Group 3 versus Group 1 or 2). In contrast, the AF in intact discs experienced greater circumferential strains than the AF in annular ring specimens. Taken together, the decrease in radial strains and increase in circumferential strains in the AF of intact discs are likely due to the increase in intradiscal pressure as the NP absorbs water and increases its volume. Importantly, AF strain distribution reported here was similar to previous observations on blood vessels, which have a uniform residual strain distribution throughout wall thickness when pressurized (Chuong and Eason, 1986). Residual strains in cardiovascular tissues are thought to be important for maintaining homeostasis during growth and remodeling (Cardamone et al., 2009; Fung, 1991; Rachev and Greenwald, 2003). Similarly, loss of NP pressurization due to degradation of proteoglycans in the NP and inner AF leads to morphological changes in disc properties commonly reported for degenerated discs, including a reduced disc height and inward bulging of the inner AF (Yang and O'Connell, 2019).

Because of the lack of vasculature in the disc, fluid flow *in vivo* primarily occurs either through the AF or through the cartilaginous endplates (Urban et al., 1977). The boundary constraints used in this study did not simulate physiological conditions, as fluid flow for the intact discs in this study was only allowed to occur through the AF periphery and axial deformations were fixed to prevent out-of-plane motion during swelling. The main purpose of this study was not to replicate *in vivo* fluid flow, but to provide mechanistic insights into the role of physical and fluid-based boundary constraints on time-dependent swelling behavior. Regardless, our study design has a few limitations, which might have influenced the quantitative results reported in this study. In the second set of experiments, surface strains likely differ from internal strains due to friction between the specimen and glass plate.

Additionally, gradual GAG leaching during swelling likely decreased the transient and equilibrium swelling ratios of tissue explants. NP and AF tissue explants were previously observed to lose ~50% of their GAG during free swelling, caused by increased pore size with water absorption (Bezci et al., 2019; Werbner et al., 2019). Due to limited knowledge of GAG leaching from disc tissues under physical boundary constraints, we quantified the amount of GAG leaching from the NP, IAF, and OAF of discs tested in the second study (Supplemental Material, Table S1). AF GAG content after swelling was ~50%–60% lower than GAG content of fresh tissue (Bezci et al., 2019). No significant decrease in NP GAG content was observed with swelling due to boundary constraints ($p > 0.05$). We expect the confounding effect of GAG leaching on tissue swelling behavior to be small given that disc tissues can retain a high water content despite large decreases in GAG content (Werbner et al., 2019; Bezci et al., 2019). Although GAG leaching is unavoidable in experimental studies, future computational studies can provide further insight into this phenomenon. Despite these limitations, radial trends

observed in this study were comparable to the trends reported by computational models (Yang and O'Connell, 2019). However, differences in axial-direction boundary conditions likely caused the differences in strain magnitudes between computational models and experiments. That is, model simulations were allowed to deform freely in the axial direction, but experimental data were collected with fixed physical boundary condition in the axial direction to prevent out-of-plane tissue swelling. These differences may be due in part to comparing finite element predictions for human discs with experimental measurements on bovine discs, as human lumbar and bovine caudal discs differ in geometric shape and composition (O'Connell, 2007). Strain patterns for human discs are different in anterior and posterior directions largely due to kidney bean shape, in contrast to bovine discs, which are more circular and similar in composition (Yang and O'Connell, 2019).

Removing the disc from surrounding endplates decreased the internal stress and caused water to flow into the tissue against the osmotic gradient until a new equilibrium was established. In free swelling conditions, NP tissue explants increased their weight by two-fold due to water absorption. However, the swelling capacity of the NP was largely reduced when swelling was restricted to occur only in the radial direction or constrained by the surrounding AF. As expected, the swelling ratio of the AF rings was much smaller than the swelling ratio of the NP explants due to structural and compositional differences. The swelling of the AF rings in free and in-plane swelling experiments was largely restricted due to the circumferential continuity in the structure. Larger AF swelling ratio and strains would be expected if AF rings were further sectioned and tested in smaller segments. The presence of the NP in the intact discs (Group 3) reduced peak radial strains in the AF and resulted in uniform strain distribution throughout the AF. In conclusion, tissue swelling is a slow time-dependent process that is strongly modulated by tissue-specific biochemical properties and physical boundary constraints.

Author contributions

Semih Bezci: Conceptualization, Methodology, Software, Data collection and analysis, Writing, Project administration; **Kyelo Torres**: Software, Validation, Data collection and analysis, Writing; **Carlo Carraro**: Data collection, Writing, Provision of resources; **Dominic Chiavacci**: Software, Data collection and analysis, Writing; **Grace D. O'Connell**: Supervision, Provision of resources, Writing, Funding acquisition.

Declaration of competing interest

The authors declare that they have no known competing financial interests or personal relationships that could have appeared to influence the work reported in this paper.

Acknowledgements

This study was supported by funds from the National Science Foundation (NSF) CAREER Award #1751212.

Supplemental material

To quantify the GAG leaching from disc samples in the second study, dry tissue chunks collected from each disc was digested in papain solution at 60 °C for 16 h (n = 5/group). Sulphated glycosaminoglycan (s-GAG) content was measured using the 1,9-dimethylene blue dye-binding (DMBB) assay. s-GAG measurements from the swollen NP and AF tissue were normalized to dry tissue weights and compared to the pre-swollen s-GAG content reported in our previous study (Bezci et al., 2019).

Table S1
s-GAG content of swollen disc tissues in 2D swelling experiments

Test group	Disc region	s-GAG content (mg/g) Mean (Min-Max)	Range from Bezci et al., 2019 (mg/g)
Group 1: AF with center flow	IAF	73 (43–101)***	180 (66–284)
	OAF	30 (18–81)*	77 (4–180)
Group 2: AF without center flow	IAF	82 (37–154)***	180 (66–284)
	OAF	15 (11–18)**	77 (4–180)
Group 3: Whole disc	NP	360 (280–426)	341 (223–481)
	OAF	21 (13–47)*	77 (4–180)

Note: IAF: Inner Annulus Fibrosus, OAF: Outer Annulus Fibrosus, NP: Nucleus Pulposus. "*" represents statistical significance at $p < 0.05$, "**" represents statistical significance at $p < 0.01$, and "***" represents statistical significance at $p < 0.001$ (Student's t-test).

References

Antoniou, J., Steffen, T., Nelson, F., Winterbottom, N., Hollander, A.P., Poole, R.A., Alini, M., 1996. The human lumbar intervertebral disc: evidence for changes in the biosynthesis and denaturation of the extracellular matrix with growth, maturation, ageing, and degeneration. The Journal of clinical investigation 98, 996–1003.
Bezci, S.E., Nandy, A., O'Connell, G.D., 2015. Effect of Hydration on Healthy Intervertebral Disk Mechanical Stiffness. J Biomech Eng 137, 101007.
Bezci, S.E., O'Connell, G.D., 2018. Osmotic Pressure Alters Time-dependent Recovery Behavior of the Intervertebral Disc. Spine (Phila Pa 1976) 43, E334–E340.
Bezci, S.E., Werbner, B., Zhou, M., Malollari, K.G., Dorlhiac, G., Carraro, C., O'Connell, G.D., 2019. Radial variation in biochemical composition of the bovine caudal intervertebral disc. JOR Spine 2, e1065.
Botsford, D.J., Esses, S.I., Ogilvie-Harris, D.J., 1994. In vivo diurnal variation in intervertebral disc volume and morphology. Spine (Phila Pa 1976) 19, 935–940.
Cardamone, L., Valentin, A., Eberth, J.F., Humphrey, J.D., 2009. Origin of axial prestretch and residual stress in arteries. Biomech Model Mechanobiol 8, 431–446.
Chuong, C.J., Fung, Y.C., 1986. On residual stresses in arteries. J Biomech Eng 108, 189–192.
Cortes, D.H., Jacobs, N.T., DeLucca, J.F., Elliott, D.M., 2014. Elastic, permeability and swelling properties of human intervertebral disc tissues: A benchmark for tissue engineering. J Biomech 47, 2088–2094.
Duclos, S.E., Michalek, A.J., 2017. Residual strains in the intervertebral disc annulus fibrosus suggest complex tissue remodeling in response to in-vivo loading. J Mech Behav Biomed Mater 68, 232–238.
Fung, Y.C., 1991. What are the residual stresses doing in our blood vessels? Ann Biomed Eng 19, 237–249.
Iatridis, J.C., MacLean, J.J., O'Brien, M., Stokes, I.A., 2007. Measurements of proteoglycan and water content distribution in human lumbar intervertebral discs. Spine (Phila Pa 1976) 32, 1493–1497.
Inoue, H., 1981. Three-dimensional architecture of lumbar intervertebral discs. Spine (Phila Pa 1976) 6, 139–146.
Jim, B., Steffen, T., Moir, J., Roughley, P., Haglund, L., 2011. Development of an intact intervertebral disc organ culture system in which degeneration can be induced as a prelude to studying repair potential. Eur Spine J 20, 1244–1254.
Lionello, G., Sirieix, C., Baleani, M., 2014. An effective procedure to create a speckle pattern on biological soft tissue for digital image correlation measurements. J Mech Behav Biomed Mater 39, 1–8.

MacLean, J.J., Owen, J.P., Iatridis, J.C., 2007. Role of endplates in contributing to compression behaviors of motion segments and intervertebral discs. J Biomech 40, 55–63.
Marchand, F., Ahmed, A.M., 1990. Investigation of the laminate structure of lumbar disc anulus fibrosus. Spine (Phila Pa 1976) 15, 402–410.
Martin, J.T., Oldweiler, A.B., Spritzer, C.E., Soher, B.J., Erickson, M.M., Goode, A.P., DeFrate, L.E., 2018. A magnetic resonance imaging framework for quantifying intervertebral disc deformation in vivo: Reliability and application to diurnal variations in lumbar disc shape. J Biomech 71, 291–295.
Michalek, A.J., Gardner-Morse, M.G., Iatridis, J.C., 2012. Large residual strains are present in the intervertebral disc annulus fibrosus in the unloaded state. J Biomech 45, 1227–1231.
O'Connell, G.D., Jacobs, N.T., Sen, S., Vresilovic, E.J., Elliott, D.M., 2011. Axial creep loading and unloaded recovery of the human intervertebral disc and the effect of degeneration. J Mech Behav Biomed Mater 4, 933–942.
O'Connell, G.D., Vresilovic, E.J., Elliott, D.M., 2007. Comparison of animals used in disc research to human lumbar disc geometry. Spine (Phila Pa 1976) 32, 328–333.
Oftadeh, R., Connizzo, B.K., Nia, H.T., Ortiz, C., Grodzinsky, A.J., 2018. Biological connective tissues exhibit viscoelastic and poroelastic behavior at different frequency regimes: Application to tendon and skin biophysics. Acta Biomater 70, 249–259.
Parkes, M., Cann, P., Jeffers, J., 2017. Real-time observation of fluid flows in tissue during stress relaxation using Raman spectroscopy. J Biomech 60, 261–265.
Perie, D.S., Maclean, J.J., Owen, J.P., Iatridis, J.C., 2006. Correlating material properties with tissue composition in enzymatically digested bovine annulus fibrosus and nucleus pulposus tissue. Ann Biomed Eng 34, 769–777.
Rachev, A., Greenwald, S.E., 2003. Residual strains in conduit arteries. J Biomech 36, 661–670.
Reitmaier, S., Shirazi-Adl, A., Bashkuev, M., Wilke, H.J., Gloria, A., Schmidt, H., 2012. In vitro and in silico investigations of disc nucleus replacement. J R Soc Interface 9, 1869–1879.
Schmidt, H., Shirazi-Adl, A., Schilling, C., Dreischarf, M., 2016. Preload substantially influences the intervertebral disc stiffness in loading-unloading cycles of compression. J Biomech 49, 1926–1932.
Schroeder, Y., Wilson, W., Huyghe, J.M., Baaijens, F.P., 2006. Osmoviscoelastic finite element model of the intervertebral disc. Eur Spine J 15 Suppl (3), S361–371.
Tavakoli, J., 2017. Region-media coupling in characterization and modelling of the disc annulus single lamella swelling. Med Biol Eng Comput 55, 1483–1492.
Urban, J.P., Holm, S., Maroudas, A., Nachemson, A., 1977. Nutrition of the intervertebral disk. An in vivo study of solute transport. Clin Orthop Relat Res 101–114.
Urban, J.P.G., Maroudas, A., 1981. Swelling of the intervertebral disc in vitro. Connect. Tissue Res. https://doi.org/10.3109/03008208109160234.
Urban, J.P.G., Maroudas, A., Bayliss, M.T., Dillon, J., 1979. Swelling pressures of proteoglycans at the concentrations found in cartilaginous tissues. Biorheology. https://doi.org/10.3233/BIR-1979-16609.
van der Veen, A.J., Bisschop, A., Mullender, M.G., van Dieen, J.H., 2013. Modelling creep behaviour of the human intervertebral disc. J Biomech 46, 2101–2103.
van der Veen, A.J., van Dieen, J.H., Nadort, A., Stam, B., Smit, T.H., 2007. Intervertebral disc recovery after dynamic or static loading in vitro: is there a role for the endplate? J Biomech 40, 2230–2235.
Vergroesen, P.P., van der Veen, A.J., van Royen, B.J., Kingma, I., Smit, T.H., 2014. Intradiscal pressure depends on recent loading and correlates with disc height and compressive stiffness. Eur Spine J 23, 2359–2368.
Werbner, B., Spack, K., O'Connell, G.D., 2019. Bovine annulus fibrosus hydration affects rate-dependent failure mechanics in tension. J Biomech 89, 34–39.
Yang, B., O'Connell, G.D., 2019. Intervertebral disc swelling maintains strain homeostasis throughout the annulus fibrosus: A finite element analysis of healthy and degenerated discs. Acta Biomater 100, 61–74.
Zhou, B., Ravindran, S., Ferdous, J., Kidane, A., Sutton, M.A., Shazly, T., 2016. Using Digital Image Correlation to Characterize Local Strains on Vascular Tissue Specimens. J Vis Exp e53625.
Zhou, M., Bezci, S.E., O'Connell, G.D., 2020. Multiscale composite model of fiber-reinforced tissues with direct representation of sub-tissue properties. Biomech Model Mechanobiol 19, 745–759.